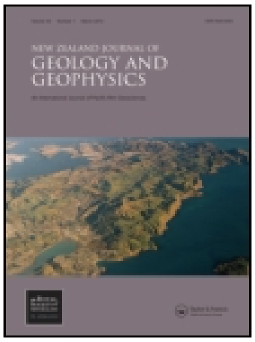

New Zealand Journal of Geology and Geophysics

ISSN: 0028-8306 (Print) 1175-8791 (Online) Journal homepage: http://www.tandfonline.com/loi/tnzg20

Fault slip models of the 2010–2011 Canterbury, New Zealand, earthquakes from geodetic data and observations of postseismic ground deformation

John Beavan , Mahdi Motagh , Eric J Fielding , Nic Donnelly & Dave Collett

To cite this article: John Beavan , Mahdi Motagh , Eric J Fielding , Nic Donnelly & Dave Collett (2012) Fault slip models of the 2010–2011 Canterbury, New Zealand, earthquakes from geodetic data and observations of postseismic ground deformation, New Zealand Journal of Geology and Geophysics, 55:3, 207-221, DOI: 10.1080/00288306.2012.697472

To link to this article: http://dx.doi.org/10.1080/00288306.2012.697472

New Zealand Journal of Geology and Geophysics
Vol. 55, No. 3, September 2012, 207–221

Fault slip models of the 2010–2011 Canterbury, New Zealand, earthquakes from geodetic data and observations of postseismic ground deformation

John Beavan[a]*, Mahdi Motagh[b], Eric J Fielding[c], Nic Donnelly[d] and Dave Collett[d]

[a]*GNS Science, Lower Hutt, New Zealand;* [b]*GFZ, Potsdam, Germany;* [c]*JPL/Caltech, Pasadena, California, USA;* [d]*Land Information New Zealand, Wellington, New Zealand*

(*Received 15 December 2011; final version received 18 May 2012*)

We present source models derived from geodetic data for the four major Canterbury earthquakes of 2010–2011. The September 2010 Darfield earthquake was largely right-lateral, but with several other fault segments active. The February 2011 Christchurch earthquake was mixed right-lateral and reverse with a left-stepping offset interrupting an ENE-striking rupture. The June 2011 earthquake included left-lateral slip on a NNW-striking fault. The December 2011 earthquakes were characterised by offshore reverse slip on an ENE-striking plane. Displacements of GPS sites define small but clearly detectable postseismic deformation east of the September 2010 earthquake, near the February 2011 earthquake and following the June 2011 earthquake. There has been no major moment release in a 15-km-long region between the eastern end of the September 2010 faulting and the western end of the February 2011 faulting. We recommend careful monitoring of this region for the next several years.

Keywords: Canterbury; earthquake; InSAR; GPS; New Zealand; source model

Introduction

The Canterbury earthquake sequence of 2010–2011 included four earthquakes with magnitude $M_W \geq 6.0$ (Fig. 1), three of which were highly damaging and one that caused more than 180 fatalities. All occurred on previously unrecognised faults. Geodetic observations, mainly GPS and satellite radar, have enabled ground deformation at the time of the earthquake (coseismic deformation) to be measured. The coseismic deformation data have been inverted to infer the fault location and fault slip distribution for the 4 September 2010 Darfield earthquake (Beavan et al. 2010b; Elliot et al. 2012) and the 22 February 2011 Christchurch earthquake (Beavan et al. 2011; Elliot et al. 2012) (all dates are given in local time). The only observed surface rupture was of the Greendale Fault during the September 2010 earthquake, with maximum right-lateral displacement of $\sim$5 m (Quigley et al. 2010, 2012; Elliot et al. 2012).

We present here updated slip models and fault locations for the September 2010 and February 2011 earthquakes and also models for the June and December 2011 earthquakes. As well as providing an understanding of the earthquakes, such models are important because they can be used to infer stress changes in the surrounding rock. They can also highlight regions where potential future earthquakes may occur, in which ongoing ground deformation observations are therefore important.

We also present GPS observations of ground deformation occurring in the September 2010–February 2011, February–June 2011 and June 2011–March 2012 intervals. Following the September earthquake there was clear (although small) ongoing right-lateral deformation (if assumed to be on east–west planes) to the east of the Greendale Fault. Following the February earthquake there was clear postseismic deformation in the vicinity of the earthquake. Regional postseismic displacements of up to 10 mm/yr have continued since the June earthquake. Work is ongoing to combine these GPS observations with satellite radar observations to better define and interpret the between-earthquakes deformation. We note here that all the mainshock and aftershock locations in this paper are from solution 2012mar11b of S Bannister (pers. comm., March 2012; updated from Bannister et al. 2011) and location uncertainties are at least 1 km.

GPS and satellite radar data, processing and modelling

The GPS data spanning the September 2010 and February 2011 earthquakes were collected and processed as described by Beavan et al. (2010b, 2011). The GPS data spanning the

---

*Corresponding author. Email: j.beavan@gns.cri.nz
Supplementary data available online at www.tandfonline.com/10.1080/00288306.2012.697472
Supplementary file 1: Figures S1–S10 Observed, modelled and residual satellite radar images used in the earthquake source modelling; **Supplementary file 2:** Tables 1–4 Observed and modelled GPS displacements; **Supplementary file 3:** Tables 5–8 Fault model parameters; **Supplementary file 4:** Table 9 Observed postseismic time series at GPS sites

ISSN 0028-8306 print/ISSN 1175-8791 online

http://dx.doi.org/10.1080/00288306.2012.697472
http://www.tandfonline.com

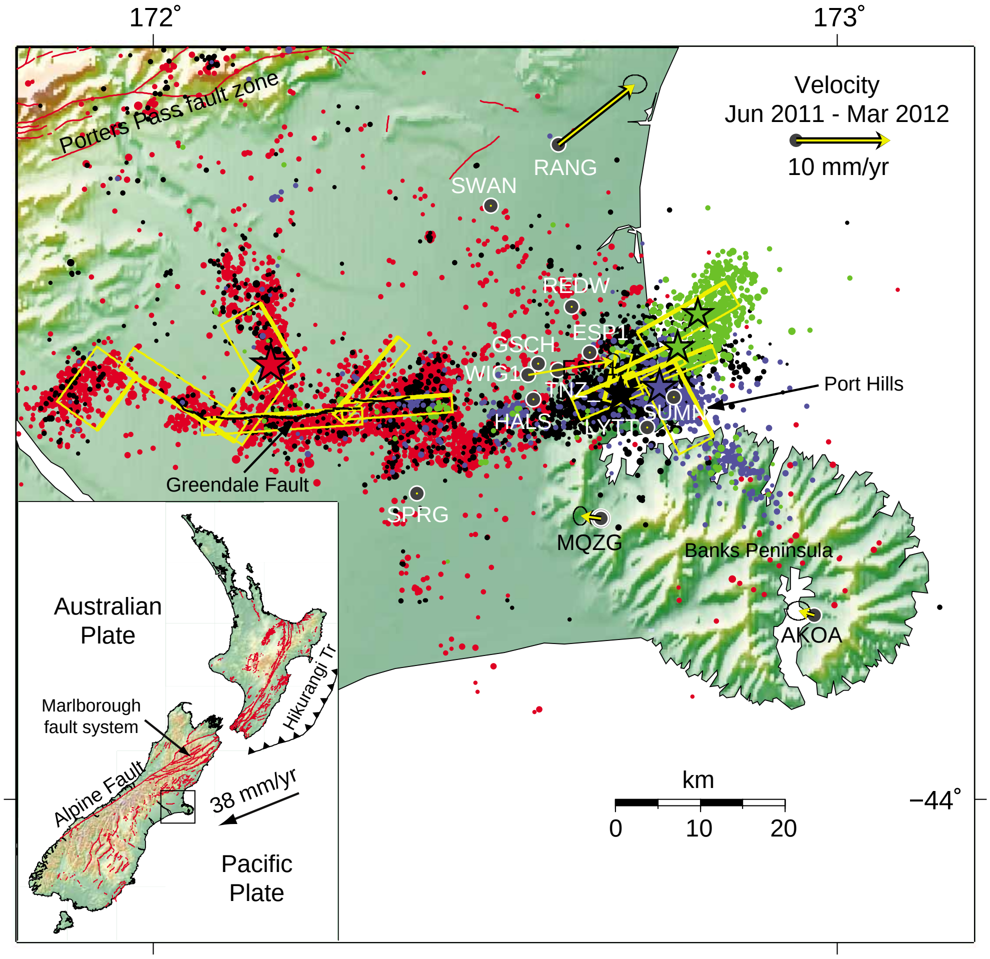

Figure 1 Epicentres, aftershocks and modelled fault planes for the ongoing 2010–2011 Canterbury earthquake sequence plus June 2011–March 2012 postseismic velocities at continuous GPS stations, on a background of shaded topography. Red, black, blue and green stars show the epicentres of the 4 September 2010 (M_W 7.2), 22 February 2011 (M_W 6.2), 13 June 2011 (M_W 6.0) and 23 December 2011 (M_W 6.0 for the two largest quakes combined) earthquakes, respectively, quoting GeoNet regional moment tensor determinations of M_W. The epicentres of the two largest shocks (M_W 5.8 and 5.9) are shown for 23 December 2011. Coloured dots show the aftershocks occurring in the intervals between these main shocks (red indicates aftershocks from September 2010–February 2011, etc.). Yellow rectangles show the outlines of the fault planes inferred from geodetic data for the main shocks; the thick line indicates the top edge of each plane. See Figs 2 and 3 for more detail. Black and white circles show continuous GPS stations operating in the vicinity of Christchurch at some time during the earthquake sequence; only MQZG has a geodetic-quality ground monument. Yellow and black arrows with 68% confidence ellipses show the average velocities between June 2011 and March 2012 for the four stations currently operating, relative to their estimated velocities prior to the start of the earthquake sequence. Red lines show mapped active faults, with the newly mapped Greendale Fault surface trace as a black line. The inset shows topography, active faults (red lines) and the relative velocity between the Pacific and Australian plates near Christchurch (DeMets et al. 2010).

June 2011 earthquake were collected largely by Land Information New Zealand (LINZ) and those spanning the December 2011 earthquakes by Christchurch City Council (CCC).

We use satellite radar data processed by the Differential Interferometric Synthetic Aperture Radar (DInSAR) technique (Table 1). The data used for the September 2010 earthquake are as described by Beavan et al. (2010b), but some of the data have been reprocessed since that paper and we use only the ALOS and Envisat tracks that cover the whole earthquake region. The DInSAR data used for the February 2011 earthquake are as described by Beavan et al. (2011), except that we now include all of the ALOS DInSAR image rather than masking out a region east of central Christchurch (see figs 3 and S3 of Beavan et al. 2011), as well as range offset data from the Cosmo-SkyMed (CSK) radar satellite (fig. 4 of Beavan et al. 2011). The processing for the June and December 2011 earthquakes is as described by Beavan et al. (2011).

Since the publication of Beavan et al. (2011), a new source of data on the February 2011 earthquake has become available. This is a height difference image derived from LiDAR data collected before and after the earthquake. We

Table 1 DInSAR details.

Data type	Track	Dates (yyyymmdd)	Perpendicular baseline (m)
4 September 2010 earthquake			
ALOS asc	337	20100813 20100928	355
ENVI asc	51	20100604 20100917	111
22 February 2011 earthquake			
CSK asc	NA	20110219 20110222	20
CSK desc	NA	20110220 20110316	123
ALOS asc	336	20101027 20110314	2100
13 June 2011 earthquake			
CSK asc	NA	20110611 20110628	92
TSX desc	55	20110609 20110620	41
ENVI asc	195	20110608 20110708	44
23 December 2011 earthquakes			
CSK asc	NA	20111220 20120105	87

Note: NA, not available.

do not use the data in the inversion but we use it as a guide to the location of the faults active during the earthquake. We also compare the model predictions against the LiDAR observations as an informal check on the model.

The modelling of the DInSAR and GPS displacement data is based on the work of Jónsson et al. (2002) and follows Beavan et al. (2010a, 2010b, 2011). In brief, we choose fault plane locations using surface rupture observations, features in the DInSAR and GPS deformation fields and, to a small extent, aftershock lineations. We start by using non-linear inversions assuming uniform slip on rectangular faults in an elastic half-space to define the geometry of the fault planes. We then extend the fault planes laterally and with depth, divide each plane into 1 × 1 km patches and perform a linear inversion for variable fault slip on these planes using Laplacian smoothing with no constraints on slip direction (rake). We modestly adjust the geometry (location, strike, dip) of the fault planes by grid search and repeat the inversion to find geometries and associated slip distributions that provide improved fits to the deformation data. We also adjust the dimensions of the faults if it is apparent, for example, that little slip is modelled towards one end of a fault. Because so many fault planes ruptured near-simultaneously, especially in the September 2010 earthquake, it is not possible to rigorously search the entire parameter space.

We therefore do not claim to have found optimum solutions. Rather, they are the best solutions we have found through a judicious use of independent data, trial-and-error and formal inversion. We also do not use a formal technique for deriving the optimum smoothing parameter in the inversion; it is always obvious when the solution is much too smooth or too rough, and we use a parameter midway between these extremes. Reducing the smoothing parameter within the acceptable range gives a somewhat rougher solution and higher maximum slip.

In the case of the September earthquake, during which many separate fault planes ruptured, we test whether adding a new fault segment to the model provides a significant improvement by tabulating the goodness-of-fit as fault segments are added. However, we do not formally test the improvement because of the difficulty of correctly assigning the number of degrees of freedom in the presence of smoothing. As discussed by Beavan et al. (2011), we subjectively downweight GPS displacements that give very large residuals to the model on the grounds that these sites were probably affected by local ground failure.

All our models assume a uniform elastic half space. In reality, there is a significant increase of elastic moduli with depth in the Darfield earthquake region as the rocks change from gravels to greywacke to eclogite (Forsyth et al. 2008; Reyners et al. 2011). For the Christchurch earthquakes, there are added complications due to the presence of interleaved estuarine sediments in the upper few hundred metres and volcanic layers in the top several kilometres (Forsyth et al. 2008). In addition, there are significant lateral variations and topography due to the volcanic structures of the Banks Peninsula. The models derived here may therefore contain systematic errors that will only be corrected when a more realistic elastic structure is adopted. It is partly for this reason that we do not attempt rigorous error analyses on our derived fault slip models.

Results

For each of the earthquakes described below, the supplementary material includes tabulated values of observed and modelled GPS displacements (Supplementary file 2), tabulated dislocation model parameters (Supplementary file 3) and observed, modelled and residual satellite radar images (Supplementary file 1).

4 September 2010 earthquake

Our model for the 4 September 2010 earthquake is shown in Figs 2A and 3A–G, and a summary of the model fault parameters for this and the other earthquakes is given in Table 2. A feature of the earthquake is that most moment release occurred on the largely right-lateral Greendale Fault ([a]–[c] in Figs 2A and 3A–C), but that the rupture initiated

Table 2 Summary of model fault parameters. The calculation of moment and M_W assumes shear modulus of 3×10^{10} N/m^2 (30 GPa). Total modelled M_W for each earthquake is 7.14, 6.38, 6.18 and 6.12, respectively. Model fault segment [a] is not linear, but approximately follows the Greendale Fault surface rupture.

Segment	Strike (°)	Dip (°)	Style	Length (km)	Width (km)	Top (km)	Avg. slip (m)	Avg. rake (°)	Moment (10^{18} Nm)	M_W
4 September 2010										
a	86	80	RL	19	11	0	2.84	174	19.19	6.83
b	303	75	RL/norm	16	11	0	1.82	−165	10.04	6.64
c	86	78	RL	13	10	0	1.94	178	8.49	6.59
d	35	70	Rev	9	11	0.5	1.22	102	5.13	6.44
e	216	50	Rev	8	10	0.5	1.12	78	3.25	6.31
f	150	54	LL	9	9	1	1.34	6	3.82	6.36
g	40	80	RL	12	10	1	1.44	171	6.63	6.52
22 February 2011										
h	67	70	RL	8	8	0.5	0.63	−167	1.26	6.04
i	15	75	Rev	6	7	0.5	0.71	87	0.93	5.95
j	64	70	RL/rev	8	8	0.5	0.95	146	1.88	6.15
13 June 2011										
k	69	78	RL/rev	11	8	1	0.36	151	1.05	5.98
l	153	56	LL	10	8	1	0.38	4	1.02	5.97
23 December 2011										
m	60	69	Rev/RL	12	9	1	0.46	136	1.71	6.12

on a reverse fault ([d] in Figs 2A and 3D) several kilometres to its north (Gledhill et al. 2011). Table 3 shows the goodness-of-fit statistic (χ^2 per estimated degree of freedom or χ^2_R) as more fault segments are added to the model, to demonstrate that each segment makes a substantial contribution to improving the fit.

One difference from the model of Beavan et al. (2010b) is that we have broken the faults into 1 × 1 km rather than 2 × 2 km patches to obtain higher spatial resolution of the slip distribution. Another difference is that we have bent the model fault plane to follow the surface rupture on the central section of the Greendale Fault rather than keeping it strictly planar; this significantly reduces some of the near-fault GPS residuals.

Based on an aftershock lineation (Fig. 1) and residuals in the GPS displacements (Fig. 2A), we have identified a left-lateral fault segment trending NNW from the epicentre. A fault segment trending NE from the major left-stepping offset in the Greendale Fault, which was provisionally identified by Beavan et al. (2010b), is also indicated by the present analysis. Both these segments must have failed coseismically on 4 September 2010 (or aseismically within a few days of the earthquake) as there have been too few aftershocks in the region to account for their moment release.

A left-lateral fault segment has also been identified by Elliot et al. (2012). They used sub-pixel offset analyses of ascending and descending ALOS radar images that provide better evidence for the left-lateral segment than the data we used. The models of Elliot et al. (2012) and the model presented here are generally similar, even though the studies did not use identical data (the main differences being that Elliot et al. included the sub-pixel offset data referred to above while we included GPS data). Further, our definitions of the Greendale Fault in terms of linear fault segments are somewhat different. The left-lateral segment referred to above is better defined by Elliot et al. and is in a somewhat different location to ours, while the segment trending NE from the major Greendale Fault stepover is not recognised by Elliot et al. The models are similar enough that stress change predictions in the surrounding crust are likely to be similar (except in the very near field).

22 February 2011 earthquake

Beavan et al. (2011) presented single-fault and two-fault models of the February earthquake, but acknowledged that a region of apparent ground uplift in eastern Christchurch

Table 3 Darfield earthquake: estimated moment magnitudes of fault segments and goodness of fit as fault segments are added.

Fault segments	M_W	χ^2_R
Greendale Fault (3 segments)	7.02	5.16
+ Charing Cross reverse	6.44	3.43
+ reverse near Hororata	6.31	2.09
+ NNW from epicentre (LL)	6.36	1.54
+ NE from stepover (RL)	6.52	0.99

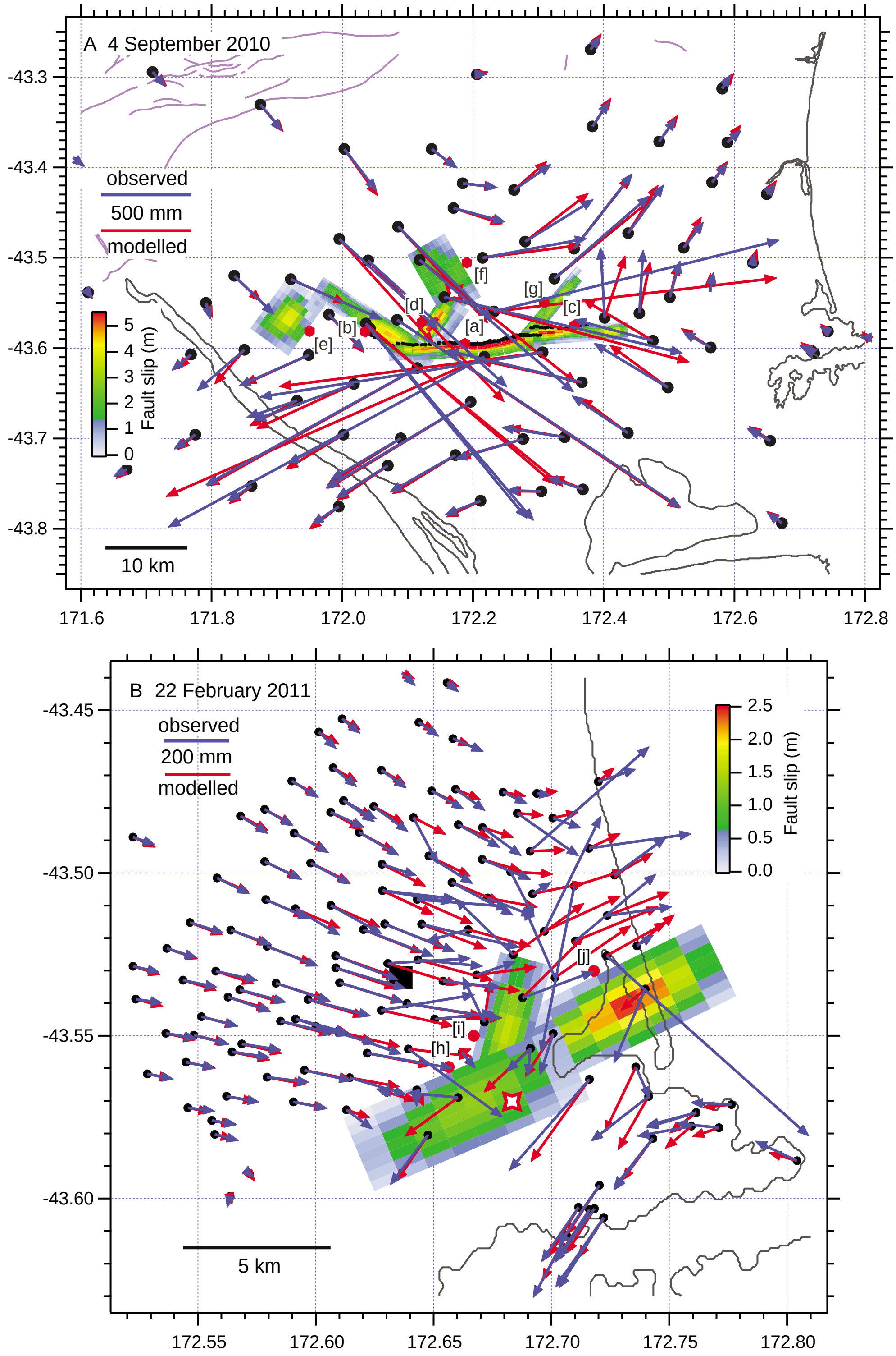

Figure 2 Observed (blue) and modelled (red) displacements at GPS sites, and the slip model derived from GPS and DInSAR data for each of the major Canterbury earthquakes. **A**, 4 September 2010; **B**, 22 February 2011; **C**, 13 June 2011; and **D**, 23 December 2011. Red dots with nearby letters in square brackets (e.g. [a]) are located where the centres of the fault segments would outcrop if extended to the surface. Detailed slip distributions on each fault segment ([a], [b], [c], etc.) are shown in Fig. 3. Some observed GPS displacements have large residuals to the model, particularly for the February 2011 earthquake, and these are downweighted in the inversion. Red and white four-pointed stars show epicentral locations from solution 2012mar11b of S. Bannister (pers. comm. 2012: updated from Bannister et al. 2011). Black square in B shows central Christchurch.

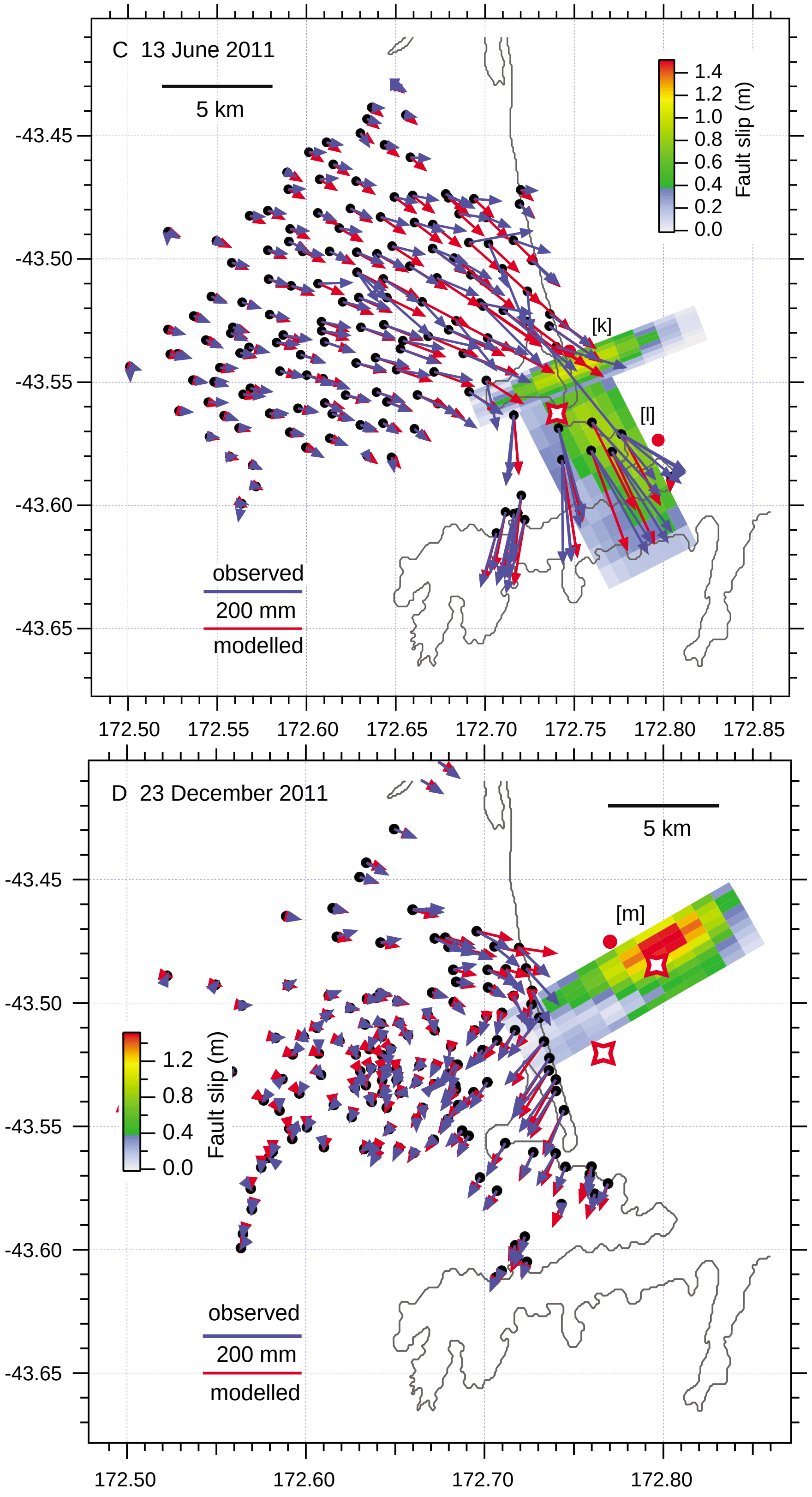

Figure 2 (*Continued*).

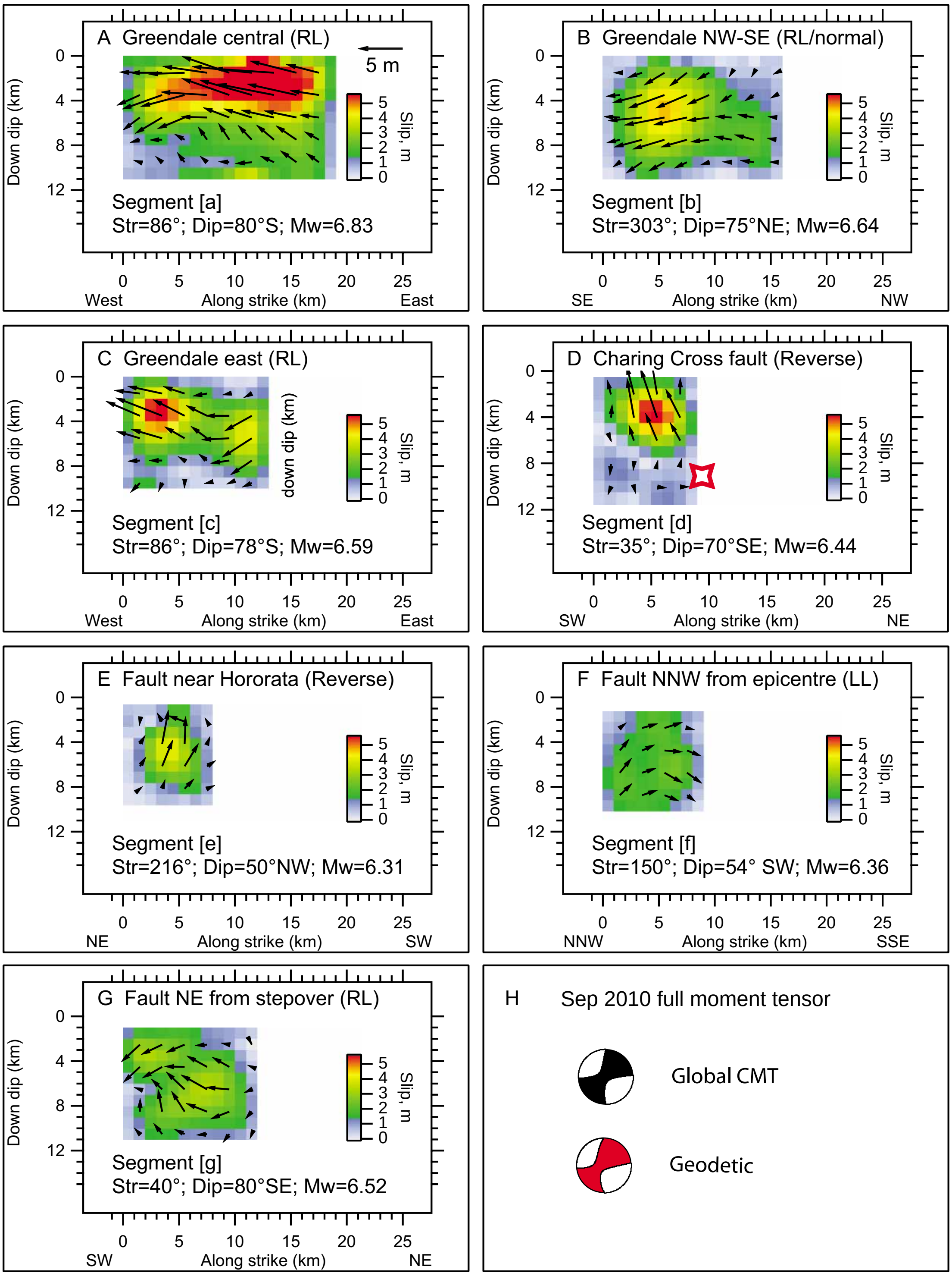

Figure 3 Slip magnitude and direction on each of the fault segments modelled as active during the earthquake sequence to date. **A–G**, **I–K**, **M–O**, labels [a]–[m] correspond to the fault segment labels in Fig. 2. The faults are discretised into 1 × 1 km patches. Slip vectors showing the motion of the hanging wall relative to the footwall are shown on every other patch. The red-and-white four-pointed stars show hypocentral locations projected onto nearby fault planes. Panels **H, L** and **P** compare the moment tensors from the sum of the fault segments contributing to each earthquake with the GCMT seismological moment tensor solution and the GeoNet regional moment tensor solution. Full moment tensor solutions are shown for the September 2010 and February 2011 earthquakes and double-couple solutions for the less well-constrained June 2011 and December 2011 earthquakes. The velocity scale arrows in panels **A, I** and **M** apply to panels **A–G**, **I–K** and **M–O**, respectively.

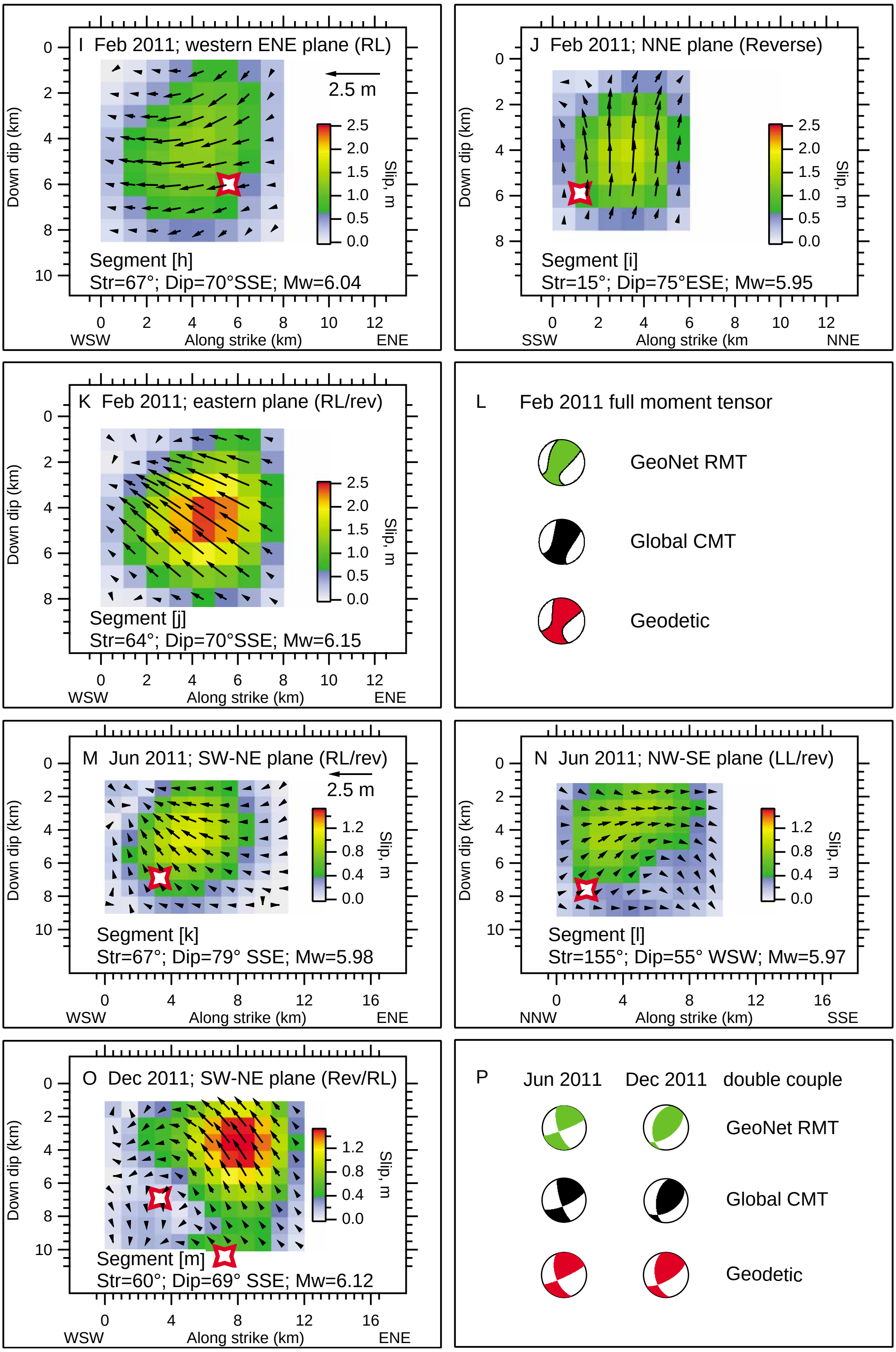

Figure 3 (*Continued*).

was not fit by their models. Elliot et al. (2012) presented a two-fault model of the earthquake based on a variety of satellite radar data, with both faults dipping SE or ESE. This model provides a reasonable fit to the eastern Christchurch uplift region and to the overall deformation field. Based on newly available data, we present a model that we believe to be a better fit than that obtained by Elliot et al. (2012).

LiDAR data were acquired over Christchurch following all three earthquakes and have been compared to earlier (2003–2005) LiDAR data collected for other purposes. A Digital Elevation Model (DEM) can be derived from each dataset, and these can be differenced to provide an estimate of vertical displacement during each earthquake. The post-September 2010 LiDAR survey did not cover the southern part of the city where much of the February 2011 deformation took place. The best coverage of the February deformation is therefore obtained by differencing the 2003 LiDAR with that obtained in May 2011. A highly smoothed portion of this DEM difference is plotted in Fig. 4A. It clearly shows the region of uplift west of the Avon–Heathcote Estuary (Fig. 4A) that is also seen in ALOS DInSAR and CSK sub-pixel correlation images (figs 3 and 4 of Beavan et al. 2011).

Figures 4B–C show two profiles across the boundary of the uplift region. These profiles resemble fault scarps and suggest that these boundaries indicate the locations of faults on which slip has propagated almost to the surface. Given the three months that elapsed between the earthquake and the LiDAR data collection in May 2011, the fault slip to these shallow depths may not have been coseismic but may have propagated through the top several hundred metres of estuarine sediments in the intervening time. Regardless, the LiDAR profiles suggest an ENE-trending fault with a left-stepping offset. We model this as three fault segments with the result shown in Figs 2B and 3I–K. The eastern section of faulting is oblique reverse/right-lateral, the western section is mainly right-lateral and the NNE-trending cross-fault is nearly pure reverse.

As an aside, the LiDAR data have ‘striping’ artefacts in an ENE direction due to poor control of the aircraft attitude in one or other of the surveys. This means that profile A–A’ on Fig. 4 may be affected by these artefacts. Profile B-B’ however, which is the more important profile for indicating the presence of the NNE-trending cross-fault, is not so affected.

This model has a better goodness of fit ($\chi^2_R = 2.09$) than our own implementation of Elliot et al.’s (2012) model ($\chi^2_R = 2.91$). To provide fair χ^2_R comparisons, we used identical data, dataset weightings and smoothing parameters in each of the models. It is difficult to argue that our model is better in a statistically significant sense than Elliot et al.’s (2012) model because we used three fault planes rather than two and we cannot accurately assess the number of degrees of freedom given the smoothing inherent in the inversion. We think, however, that the LiDAR evidence for possible fault scarps argues in favour of our model. Planes [h] and [i] of our model are similar to the two planes modelled for this earthquake by Elliot et al. (2012), but in our analysis plane [j] is also required and carries more of the moment than either of the other planes.

A note regarding the two-fault solution of Beavan et al. (2011) is required. In that work, we argued that the second fault might have been due to two large aftershocks that occurred within 4 hours of the main shock. We justified this interpretation on the grounds that the inferred moment of the second fault (M_W 5.95) was comparable with that of the magnitude 5.8 and 5.9 aftershocks combined. However, we mistakenly described these magnitudes as M_W when they are in fact M_L magnitudes recorded by GeoNet, which are typically 0.2–0.3 units higher than M_W for this earthquake sequence. Indeed, the Global CMT project assigns these aftershocks magnitudes of M_W 5.5 and 5.6. Therefore, if slip did occur on the second plane of the Beavan et al. (2011) model, it must have occurred during the main shock and was not due to these aftershocks. To some extent this is a moot point however, as we consider the model in this paper to be superior to either of the models given by Beavan et al. (2011).

13 June 2011 earthquake

Preliminary inversions of the June coseismic displacement data suggested that the earthquake occurred at least partially offshore, making it harder to obtain a reliable solution because of the lack of offshore geodetic data. Nevertheless, the pattern of GPS displacements in the eastern Port Hills (Fig. 1) required the rupture to have included left-lateral slip on a NNW-trending fault plane. This finding is also consistent with a NW trend of aftershocks leading from the earthquake location across Banks Peninsula (Bannister et al. 2011; Fig. 1). No ENE-trending fault model could explain these GPS observations, nor could they be due to aftershocks because the moment release in the aftershocks was far too small.

Two possibilities were investigated. One was that the earthquake occurred entirely on a NNW-trending fault. The other was that two faults were involved, one trending ENE and the other NNW. In the single-fault model (not shown) the slip almost resolves into two patches on a WSW-dipping fault, a deeper oblique reverse/left-lateral patch near the northern end of the rupture and a shallower left-lateral patch near the southern end. In the two-fault model the shallow left-lateral patch to the south is similar, while the northern patch is resolved as oblique reverse/right-lateral slip on a SSE-dipping fault (Figs 2C, 3M, 3N). We are currently unable to discriminate between these options. Occam’s Razor would suggest the single-fault model but the fact that the slip almost resolves into two patches makes the two-fault model seem plausible, especially when the fault

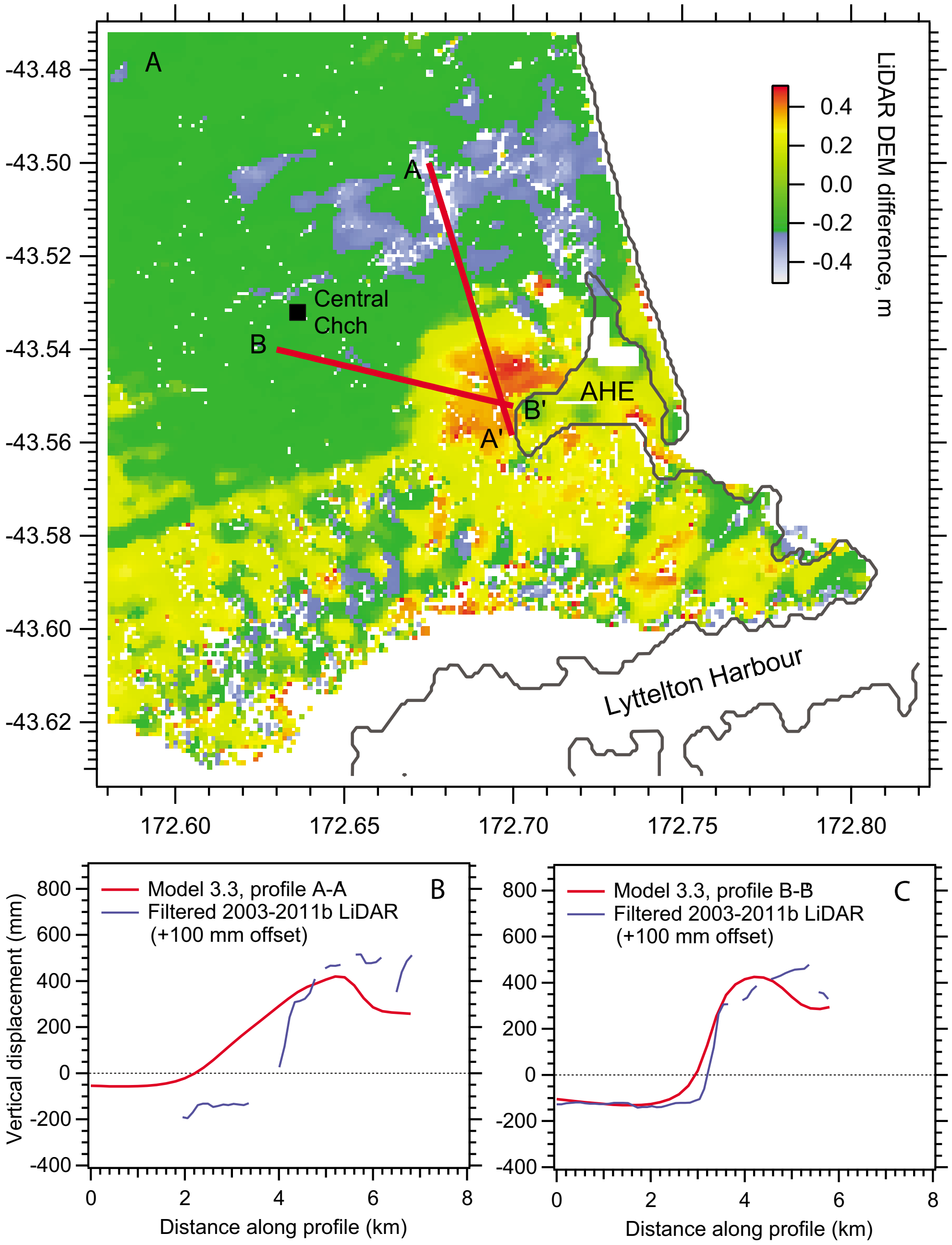

Figure 4 Difference between LiDAR DEM models generated from data acquired in 2003 and in May 2011. **A**, Smoothed portion of the LiDAR DEM difference highlighting an area of uplift west of the Avon–Heathcote Estuary (AHE). **B** and **C**, the observed (blue) and modelled (red) height changes along profiles A–A' and B–B', respectively. In the profiles we have added 100 mm to the observed data. The origin of this could be the ~50 mm subsidence in the region caused by the Darfield earthquake and/or uncertainties in the LiDAR height datum.

complexity observed in the September and February earthquakes is considered.

23 December 2011 earthquakes

Seismological locations for the sequence of earthquakes on 23 December show that these earthquakes occurred largely offshore. However, onshore displacements were observed with both GPS (Fig. 2D) and satellite radar data that enabled us to find a fault slip solution. The western end of the faulting is better constrained by the available data than the faulting further offshore, which shows a mainly reverse slip patch centred 7–8 km offshore and at 3–4 km depth (Figs 2D, 3O).

Postseismic deformation

Postseismic deformation derived from DInSAR data following the Darfield earthquake has been presented by several authors at conferences and on websites. Here we concentrate on the deformation recorded by continuous GPS (cGPS) sites in the region east of the Greendale Fault. As well as showing postseismic deformation in their own right, these data can be used to constrain time series of DInSAR images that may be affected by orbital and atmospheric errors at low levels of deformation. There is only one geodetic-quality cGPS station in this region (MQZG; Fig. 1) but, fortuitously, a number of sites were operated by commercial interests over part of the time interval. These data were intended for real-time networks so the operators did not routinely archive the data. At our request however, they did their best to retrieve as much data as possible.

Figure 1 shows the locations of the sites and Fig. 5 indicates the time periods over which they were operating. Table 9 in Supplementary file 4 gives numerical values for the cGPS time series. Six of the sites were operated by Trimble New Zealand (TNZ), whose buildings were damaged by fire in mid-May 2011 destroying the servers that operated the network. As well as being unfortunate for TNZ, this was most unfortunate for monitoring deformation leading up to the June earthquake; archiving of the TNZ network was not re-established until February 2012.

We process the cGPS data to daily solutions in the ITRF2008/IGS08 reference frame using standard double-difference techniques. We subtract from each time series the velocity predicted by the New Zealand national deformation model (updated after Beavan and Haines 2001 using 1996–2009 GPS data). These velocities vary by only ±1 mm/yr over the region of interest. The horizontal velocity at MQZG in the year prior to the Darfield earthquake differs from zero by ~5 mm/yr. We attribute this in part to postseismic deformation following the 2009 Dusky Sound earthquake (Beavan et al. 2010a), but it may also be partly due to a regional error in the national deformation model. We subtract this velocity from all the Christchurch region cGPS time series so that they define, to the best of our ability, changes in deformation rate since the Darfield earthquake. We estimate and remove coseismic offsets at the times of significant earthquakes (Table 4) and plot the resulting time series in Fig. 5.

Only station MQZG is on a geodetic-quality monument, while the others are on buildings. We must therefore be wary of interpreting the data in case there has been damage to the building or the ground on which it is situated. Station MQZG was visually inspected following the February earthquake and showed no evidence of disturbance. Bearing this in mind, we make the following observations.

During the 5.5 months between the September 2010 and February 2011 earthquakes (and after removing coseismic steps at some stations on 26 December 2011; Table 4) there is westward and slightly northward motion of ~1.5 mm at MQZG and eastward and slightly northward motion of ~4 mm at SWAN, perhaps indicating ongoing right-lateral deformation on approximately east-west planes. Stations SUMN and SPRG, south of the subsequent February earthquake rupture, also show westward motion while stations north of the future rupture exhibit a more complex pattern. All the sites seem to show modest slowing of deformation between September 2010 and February 2011.

Table 4 Coseismic offsets subtracted from time series in Fig. 5. ESP1 (Fig. 1), which was destroyed in the February 2011 earthquake, would probably have been displaced on 26 December 2010 due to its proximity to this central-city earthquake but the long gap in the time series makes it impossible to estimate an offset.

Event/site	East (mm)	North (mm)	Up (mm)
4 September 2010			
MQZG	−119	69	14
26 December 10			
HALS	−2.5	−1	0
REDW	1	0.5	0
SUMN	−1.5	1	0
TNZ_	−6	−5	0
22 February 2011			
GSCH	132	−32	−46
HALS	75	−6	−20
MQZG	−15	−47.5	−3
REDW	99	−55	−33
SPRG	0	−5	−5
SUMN	−147.5	−54	1
SWAN	15	−9	−2
TNZ_	164	−36	−51
WIG1	108	−16	−26
16 April 2011			
SUMN	−12	3	−4
TNZ_	0	−2	0
13 June 2011			
AKOA	−3	0	0
GSCH	28	−6	−5
MQZG	−12	−22	0
RANG	2	−1	0
WIG1	22	−5	−2

Summing the moments of all aftershocks between 4 September 2010 and 22 February 2011 in the region between longitudes 172.3 and 172.62 and latitudes −43.65 and −43.52, assuming $M_W = M_L - 0.2$ and that all aftershocks represent right-lateral motion on east–west planes, the summed moment ($M_W = 5.7$) corresponds to ~100 mm slip on a 15 × 8 km fault surface. Simple dislocation models show that this maximal slip estimate could explain the observed 5.5 mm relative motion between MQZG and SWAN, although it is possible that aseismic slip could also contribute. We are working on combining the GPS displacement data with time

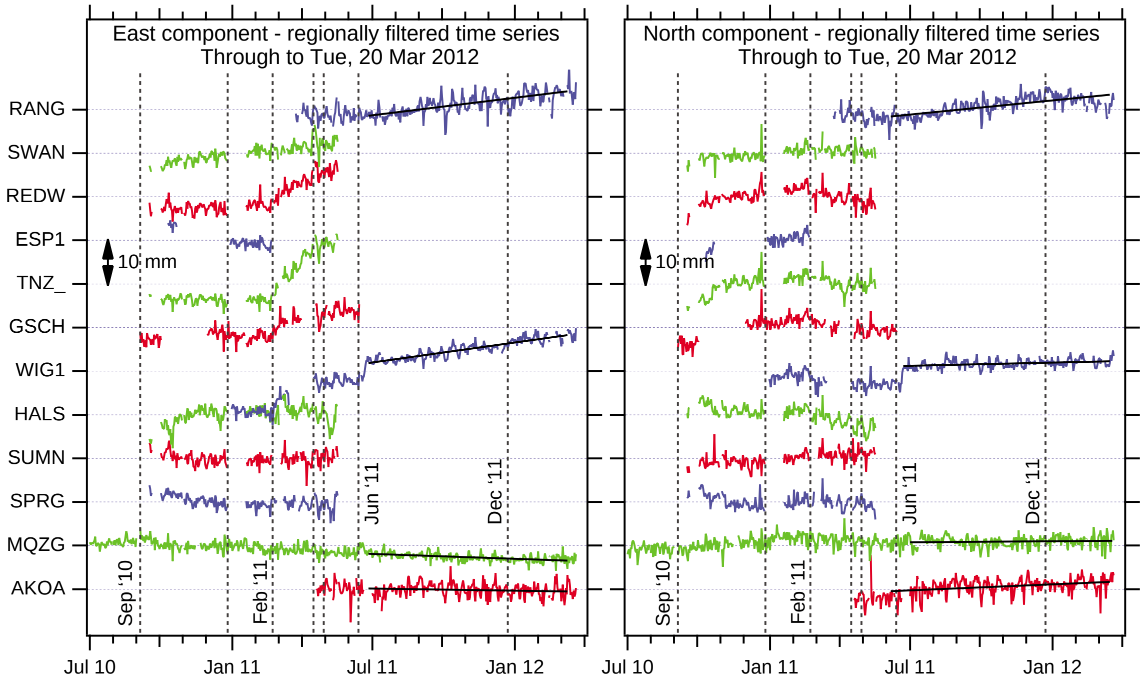

Figure 5 Time series of cGPS daily horizontal position solutions, detrended such that the horizontal velocity is zero prior to the Darfield earthquake and with estimated coseismic offsets removed (see text and Table 4). Linear fits are shown for the June 2011–March 2012 period. Not all stations were operating over the entire time period. Vertical dashed lines show the times of earthquakes that caused significant damage in Christchurch: 4 September 2010, M_W 7.2; 26 December 2010, M_L 4.9; 22 February 2011, M_W 6.2; 16 April 2011, M_L 5.3; 30 April 2011, M_L 5.2; 13 June 2011, M_W 6.0; 23 December 2011, M_W 6.0 (for the two largest quakes combined). An offset would have occurred at ESP1 during the nearby 26 December 2010 earthquake, but it has not been estimated in Table 4 because of the preceding gap in the time series. An offset that we believe to be artificial occurred at WIG1 a week after the June 2011 earthquake.

series of DInSAR images to generate a better estimate of Darfield postseismic deformation.

During the 4 months between the February and June earthquakes (and after removing intervening coseismic steps at some stations; Table 4) there are significant eastward and southward displacements at sites near the central city. These reach 10 mm or more over the first two months, then decay to low rates prior to the June earthquake. We do not know whether these displacements are due to afterslip on faults or to ongoing ground failure. The fact that nearby sites (e.g. WIG1 and GSCH) exhibit similar behaviour suggests that the deformation is due either to afterslip or to fairly widespread and deep-seated ground failure. The deformation rate at TNZ_ is particularly high; it is believed that there was some damage to the building during the February earthquake so it is possible that this signal is partially the result of building deformation. About a week after the June earthquake there is a clear offset at WIG1. The antenna was not deliberately moved (J Brice, Geosystems, pers. comm., 2011), but there was work being done on the roof around this time so we suspect this may be an artificial offset that should be removed from the time series. We do not seek to model the February postseismic deformation in this paper.

Following the June earthquake, MQZG continued generally westward at about the same rate (compared to its pre-Darfield level) of ~3 mm/yr. WIG1 showed an increasing displacement rate (~9 mm/yr) to the east and new station RANG demonstrated a significant rate (~10 mm/yr) to the northeast. With 9 months of data it is unlikely that the latter two are due to annual thermal or thermoelastic signals, although this is a possibility. Summing the moments of aftershocks between 13 June 2011 and 31 January 2012 in the region between longitudes 172.3 and 172.7 and latitudes −43.75 and −43.4, assuming $M_W = M_L - 0.2$ and that all aftershocks represent right-lateral motion on east–west planes, the summed moment ($M_W = 5.3$) corresponds to only ~25 mm slip on a 15 × 8 km fault surface. These aftershocks cannot explain the observed post-June 2011 GPS displacements, which must – if they are real – be due to aseismic slip.

We do not seek to model these signals here, but we recommend that high priority be given to continued and improved geodetic monitoring in the region in an attempt to verify and understand these signals. Station AKOA may also show accelerated north-directed motion of ~3 mm/yr in the few months following the June earthquake, although it is difficult to judge this because of the limited pre-June data.

Discussion and conclusions

Fault slip solutions

Multiple fault segments failed in at least the September 2010 and February 2011 earthquakes. The character of the faulting resembles an intraplate situation; the fault surfaces have not moved for a very long period, so that they rupture more like intact rock than the smoother rupture typical of a well-developed plate-boundary fault (e.g. Cao and Aki 1986; Kanamori and Allen 1986; Scholz et al. 1986). Because of this complexity it is difficult to find a unique solution for the fault geometry and slip distribution, as evidenced by the somewhat different models derived by Elliot et al. (2012) and in this paper. The high ratio of slip to fault length suggests high stress drop, which is also a feature of rarely active faults (e.g. Scholz et al. 1986; Fry and Gerstenberger 2011).

The majority of slip occurs in the 2–6 km depth range for most modelled fault segments, raising the question of how stress is being relieved at shallower and deeper depths. An apparent decrease of coseismic slip towards the surface has been measured geodetically in a number of other cases (e.g. Fialko et al. 2005) and possibly explained as shallow distributed slip through the earthquake cycle (Kaneko and Fialko 2011). Fielding et al. (2009) interpreted postseismic deformation after the 2003 Bam earthquake in Iran as consistent with distributed coseismic shear in the shallow sedimentary layers causing coseismic dilatancy and post-seismic recovery. Oskin et al. (2012) also presented evidence from LiDAR differencing for distributed deformation at shallow depths during or shortly after the 2010 El Mayor-Cucapah earthquake. The Canterbury Plains sedimentary layers may have similar distributed deformation causing an apparent lack of slip in geodetic modelling. However, the decrease to small values below ~6 km depth is mysterious given that the brittle–ductile transition is expected to be substantially deeper than this (Reyners and Cowan 1993; Reyners et al. 2011).

Comparison with seismological CMT solutions

In Figs 3H, 3L, 3P we compare the moment tensor solutions derived from summing the moments on the various fault planes active in each earthquake with the seismological solutions from the Global CMT project (www.globalcmt.org; accessed April 2012) and the GeoNet regional moment tensor (RMT) solutions (www.geonet.org.nz and pers. comm. J. Ristau, April 2012; Sibson et al. 2011). For the 23 December earthquakes, the CMT and RMT solutions are the combined moment tensors of the two largest earthquakes in the sequence. Elliot et al. (2012) have made a more extensive comparison of this type for their solutions for the September and February earthquakes. Agreement between the geodetic and seismological moment tensor solutions does not prove much, as there are many ways to sum slip on individual faults to generate a particular moment tensor. However, a large disagreement would indicate something wrong with one or other (or both) solutions.

For the September 2010 and February 2011 earthquakes we find reasonably close agreement. For the June and December 2011 earthquakes we find good agreement with the double-couple component, but both the GCMT and GeoNet RMT solutions have significant non-double-couple components not seen in the geodetic solutions. This bears further investigation but may not be very significant (pers. comm. J. Ristau, April 2012); the moment tensor solutions are likely to be more uncertain for these earthquakes due to their smaller size and the geodetic solution is likely to be more uncertain due to much of the surface deformation field being offshore and therefore not available for inversion.

The GCMT moment magnitudes (M_W) of the September 2010, February 2011, June 2011 and December 2011 earthquakes are 7.0, 6.1, 6.0 and 6.0, respectively. The GeoNet RMT M_W values are 7.2, 6.2, 6.0 and 6.0. (For December 2011 we combine the moments of the two largest shocks.) The M_W values determined geodetically in this paper are 7.1, 6.4, 6.2 and 6.1 (Table 2). Using InSAR data, Elliot et al. (2012) found similar geodetic values of 7.1 and 6.4 for the September 2010 and February 2011 earthquakes. The geodetic M_W estimates include days to weeks of afterslip, depending on when the postseismic geodetic data were collected.

While the geodetic and seismological values are similar for the September 2010 event, the geodetically determined values are 0.1–0.2 units higher than the seismologically determined values for the other three earthquakes. This suggests a greater proportion of aseismic afterslip in the days following the three Christchurch earthquakes, as opposed to minimal afterslip following the Darfield earthquake. The fact that ongoing postseismic slip is evident following the February and June earthquakes (Fig. 4) supports this interpretation. (There is also the possibility that the geodetically determined values are artificially high due to trade-offs between slip on the multiple model fault planes. We would expect this effect to be strongest for the 7-segment September 2010 earthquake; however, this is the earthquake with the least difference between geodetic and seismological determinations of M_W.)

Region between September and February earthquakes

Figure 1 shows the surface projection of all fault planes we have modelled as active during the September 2010–December 2011 earthquake sequence. As noted earlier, there is a region about 15 km long between the September 2010 and February 2011 faults where significant moment release has not occurred in the present sequence. Elliot et al. (2012), among others, have also brought attention to this region. There are possible reasons why this region will not fail in an earthquake or earthquakes during the present sequence. For example, faults in this region may have failed relatively recently compared to the faults that have broken in the present sequence, so even the increases in stress due to the recent earthquakes are insufficient to cause failure.

The truth however is that we do not know whether or not this region is likely to fail in the near future and, if it did, whether it would be as a single earthquake or as several smaller earthquakes. We think it is of high importance to continue and expand ongoing geodetic (and other) monitoring of this region, in case clues to its future behaviour can be provided.

Supplementary files

Supplementary file 1: Figures 1–10 Observed, modelled and residual satellite radar images used in the earthquake source modelling

Supplementary file 2: Tables 1–4 Observed and modelled GPS displacements

Supplementary file 3: Tables 5–8 Fault model parameters

Supplementary file 4: Table 9 Observed postseismic time series at GPS sites

Acknowledgements

We thank the Japanese, European, Italian and German space agencies for ALOS, Envisat, CSK and TSX satellite radar data, respectively; the New Zealand government for LiDAR data; Christchurch City Council for GPS ground displacements for the 23 December 2011 earthquakes; and Geosystems Ltd, Trimble New Zealand Ltd, Global Survey Ltd and GeoNet for providing cGPS data. We thank three anonymous reviewers and associate editor John Townend, whose comments have helped us improve the paper. JB has been supported by New Zealand government funding of the 'Tectonics and Structure of Zealandia' programme and by the New Zealand Earthquake Commission. Part of the research described in this paper was sponsored by NASA's Earth Surface and Interior focus area and performed at the Jet Propulsion Laboratory, California Institute of Technology.

References

Bannister S, Fry B, Reyners M, Ristau J, Zhang H 2011. Fine scale relocation of aftershocks of the 22 February M_W 6.2 Christchurch earthquake using double-difference tomography. Seismological Research Letters 82: 839–845. doi: 10.1785/gssrl.82.6.839

Beavan J, Haines J 2001. Contemporary velocity and strain-rate fields of the Pacific-Australian plate boundary zone through New Zealand. Journal of Geophysical Research 106: 741–770.

Beavan J, Samsonov S, Denys P, Sutherland R, Palmer N, Denham M 2010a. Oblique slip on the Puysegur subduction interface in the 2009 July M_W 7.8 Dusky Sound earthquake from GPS and InSAR observations: implications for the tectonics of southwestern New Zealand. Geophysical Journal International 183(3): 1265–1286. doi: 10.1111/j.1365-246X.2010.04798.x

Beavan J, Samsonov S, Motagh M, Wallace L, Ellis S, Palmer N 2010b. The Darfield (Canterbury) earthquake: geodetic observations and preliminary source model. Bulletin of the New Zealand Society for Earthquake Engineering 43(4): 228–235.

Beavan J, Fielding E, Motagh M, Samsonov S, Donnelly N 2011. Fault location and slip distribution of the 22 February 2011 MW 6.2 Christchurch, New Zealand, earthquake from geodetic data. Seismological Research Letters 82: 789–799. doi: 10.1785/gssrl.82.6.789

Cao T, Aki K 1986. Effect of slip rate on stress drop. Pure and Applied Geophysics 124(3): 515–529. doi: 10.1007/BF00877214

DeMets C, Gordon RG, Argus DF 2010. Geologically current plate motions. Geophysical Journal International 181(1): 1–80. doi: 10.1111/j.1365-246X.2009.04491.x

Elliot JR, Nissen EK, England PC, Jackson JA, Lamb S, Li Z, Oehlers M, Parsons B 2012. Slip in the 2010–2011 Canterbury earthquakes, New Zealand. Journal of Geophysical Research, 117: B03401. doi: 03410.01029/02011jb008868

Fialko Y, Sandwell D, Simons M, Rosen P 2005. Three-dimensional deformation caused by the Bam, Iran, earthquake and the origin of shallow slip deficit. Nature 435: 295–299. doi: 10.1038/nature03425

Fielding EJ, Lundgren PR, Bürgmann R, Funning GJ 2009. Shallow fault-zone dilatancy recovery after the 2003 Bam earthquake in Iran. Nature 458: 64–68.

Forsyth PJ, Barrell DJA, Jongens R 2008. Geology of the Christchurch area. Institute of Geological and Nuclear Sciences 1:250,000 Geological Map 16, 1 sheet + 67 p. Lower Hutt, New Zealand, GNS Science.

Fry B, Gerstenberger M 2011. Large apparent stresses from the Canterbury earthquakes of 2010 and 2011. Seismological Research Letters 82: 833–838. doi: 10.1785/gssrl.82.6.833

Gledhill K, Ristau J, Reyners M, Fry B, Holden C 2011. The Darfield (Canterbury, New Zealand) M_W 7.1 earthquake of September 2010: A preliminary seismological report. Seismological Research Letters 82(3): 378–38. doi: 10.1785/gssrl.82.3.378

Jónsson S, Zebker H, Segall P, Amelung F 2002. Fault slip distribution of the Hector Mine earthquake estimated from satellite radar and GPS measurements. Bulletin of the Seismological Society of America 92: 1377–1389.

Kanamori H, Allen CR 1986. Earthquake repeat time and average stress drop. In: Das S, Boatwright J, Scholz CH, eds, Maurice Ewing volume 6, Earthquake Source Mechanics, Washington DC, USA, American Geophysical Union. Pp. 227–235.

Kaneko Y, Fialko Y 2011. Shallow slip deficit due to large strike-slip earthquakes in dynamic rupture simulations with elasto-plastic off-fault response. Geophysical Journal International 186: 1389–1403. doi: 10.1111/j.1365-246X.2011.05117.x

Oskin ME, Arrowsmith JR, Corona AH, Elliott AJ, Fletcher JM, Fielding EJ, Gold PO, Garcia JJG, Hudnut KW, Liu-Zeng J, Teran OJ 2012. Near-Field Deformation from the El Mayor-Cucapah Earthquake Revealed by Differential LIDAR. Science 335: 702–705.

Quigley M, Villamor P, Furlong K, Beavan J, Van Dissen R, Litchfield N, Stahl T, Duffy B, Bilderback E, Noble D, Barrell D, Jongens R, Cox S 2010. Previously unknown fault shakes New Zealand's South Island. EOS, Transactions American Geophysical Union 91: 469–472.

Quigley M, Van Dissen R, Litchfield N, Villamor P, Duffy B, Barrell D, Furlong K, Stahl T, Bilderback E, Noble E 2012. Surface rupture during the 2010 M_W 7.1 Darfield (Canterbury) earthquake: implications for fault rupture dynamics and seismic-hazard analysis. Geology 40(1): 55–58. doi: 10.1130/G32528.1

Reyners M, Cowan H 1993. The transition from subduction to continental collision: crustal structure in the North Canterbury region, New Zealand. Geophysical Journal International 115(3): 1124–1136.

Reyners M, Eberhart-Phillips D, Bannister S 2011. Tracking repeated subduction of the Hikurangi Plateau beneath New Zealand. Earth and Planetary Science Letters 311: 165–171. doi: 10.1016/j.epsl.2011.09.011

Scholz CH, Aviles CA, Wesnousky SG 1986. Scaling differences between large interplate and intraplate earthquakes, Bulletin of the Seismological Society of America 76: 65–70.

Sibson R, Ghisetti F, Ristau J 2011. Stress control of an evolving strike-slip fault system during the 2010–2011 Canterbury, New Zealand, earthquake sequence. Seismological Research Letters 82(6): 824–832. doi: 10.1785/gssrl.82.6.824